Advances in Geo-Energy Research

Vol. 17, No. 3, p. 196-211, 2025

Original article

Pressure diagnostics in hydraulic fracturing for unconventional completion optimization

Zhaoyang Wei[1,2], Mao Sheng[1,2]*, Jie Li[3], Bo Zhang[4], Bo Wang[3], Gensheng Li[1,2]

[1]*State Key Laboratory of Deep Geothermal Resources, China University of Petroleum, Beijing 102249, P. R. China*

[2]*Research Center for Intelligent Drilling & Completion Technology and Equipment, China University of Petroleum, Beijing 102249, P. R. China*

[3]*Oil Production Technology Research Institute, Xinjiang Oilfield Company, PetroChina, Karamay 834000, P. R. China*

[4]*Department of Civil and Environmental Engineering, University of Alberta, Edmonton AB T6G 1H9, Canada*

Keywords:
Fracture diagnostics
pressure analysis
completion optimization
unconventional reservoirs
hydraulic fracturing

Cited as:
Wei, Z., Sheng, M., Li, J., Zhang, B., Wang, B., Li, G. Pressure diagnostics in hydraulic fracturing for unconventional completion optimization. Advances in Geo-Energy Research, 2025, 17(3): 196-211.
https://doi.org/10.46690/ager.2025.09.03

Abstract:
The accurate evaluation of hydraulic fracturing performance is essential for the iterative optimization of unconventional reservoir development. In this aspect, fracturing pressure diagnostics has been recognized as a non-invasive technique that significantly reduces operational time and cost. However, pressure-based diagnostics lack a unified workflow for the evaluation of fracture complexity and area and cannot provide sufficient guidance for design optimization. Thus, this paper proposes an integrated diagnostic framework, constructed by pressure interpretation and data mining, from which the hydraulic fracture complexity and fracture area can be quantified. The normalized fracture complexity index is defined by propagation events and energy intensity extracted from wavelet-transformed pressure signals, and the fracture area is evaluated from pressure falloff analysis. Data mining is then used to optimize the fracturing parameters based on these two indices. The results show that the proposed framework effectively characterizes the stimulated fracture area and complexity and reveals their relationships with fracturing parameters and geological factors on the basis of multi-stage data from three horizontal coalbed methane wells. The stimulated fracture area is primarily determined by the fracturing fluid volume and pumping rate, while the fracture complexity is strongly regulated by the pumping rate and compressive strength of the rock. A negative correlation was detected between the fracture complexity and the main fracture area. To balance the main area and complexity of fractures, it is necessary to optimize the key fracturing parameters. This study provides a low-cost tool that can diagnose hydraulic fracturing performance and effectively optimize unconventional completion.

1. Introduction

Hydraulic fracturing diagnostics for fracture geometry, complexity and conductivity are vital to iteratively optimize fracturing parameters for unconventional oil and gas completion (Zoback and Kohli, 2019; Li et al., 2022b; Akbari et al., 2025). Currently, fracture diagnostic technologies can be categorized into four groups: Downhole monitoring including downhole video and acoustic imaging (McCormack et al., 2021; Eyinla et al., 2023), near-wellbore monitoring with distributed fiber-optic sensing (Ekechukwu and Sharma, 2021; Nayak et al., 2024), far-field surveillance including controlled-source electromagnetic monitoring and micro-seismic (Nayak et al., 2024), and pressure-based analyses. By contrast, pressure-based diagnostics have emerged as a practical, non-

Yandy Scientific Press

*Corresponding author.
E-mail address: 2023210319@student.cup.edu.cn (Z. Wei); shengmao@cup.edu.cn (M. Sheng); lj688@petrochina.com.cn (J. Li); bzhang7@ualberta.ca (B. Zhang); wangbo2016@petrochina.com.cn (B. Wang); ligs@cup.edu.cn (G. Li).

Received July 5, 2025; revised July 30, 2025; accepted August 21, 2025; available online August 26, 2025.

invasive and cost-effective alternative with strong scalability (Lei et al., 2020; Parisio et al., 2021; Childers and Wu, 2022). Pressure signals, which can be continuously recorded at the wellhead without extra hardware, inherently reflect the fracture propagation and closure behaviors, providing an efficient pathway to evaluate stimulation effectiveness in unconventional reservoirs (Liu and Ehlig-Economides, 2018; Cui et al., 2023; Wei et al., 2025).

Representative pressure-based diagnostics mainly include pressure falloff analysis, water-hammer diagnostics and real-time injection interpretation. In pressure falloff analysis, Nolte's G-function model has been widely used to estimate closure pressure and fluid leak-off (Nolte, 1979). Its applications have been extended to unconventional reservoirs with complex fracture interactions (Eltaleb et al., 2025), as well as to multi-well systems with fracture networks (Ren et al., 2019). Further developments that incorporate fracture compliance and proppant transport enable improved evaluations of effective fracture geometry and conductivity (Afagwu et al., 2022; Wei et al., 2024). Water-hammer diagnostics utilize high-frequency oscillations after shutdown to infer the fracture entry and impedance, with cepstral analysis enhancing the identification of cluster efficiency (Hu et al., 2023a; Wang et al., 2025). Real-time injection diagnostics extend Nolte's log-log framework to account for heterogeneous formations and stress-sensitive effects (Nguyen et al., 2020; Hazlett et al., 2021). Recent advances in sensors allow high-frequency wellhead monitoring up to 1,000 Hz with 0.001 MPa resolution, enabling the detection of subtle oscillations, reflections and closure signals. Hybrid approaches that integrate pressure with distributed acoustic sensing, as well as microseismic and electromagnetic imaging further improve interpretation (Hudson et al., 2021; Liu et al., 2021). However, pressure-based methods remain confined to single-phase interpretations, and there is still a lack of a systematic pressure-analysis framework that would integrate mini-frac, main injection and falloff data, thus enabling the simultaneous evaluation of fracture complexity and stimulated fracture area while establishing robust quantitative links with fracturing completion parameters.

Effective completion optimization relies on linking the monitoring results with fracturing parameters and geological factors (Tripoppoom et al., 2020; Zhang et al., 2022). Such integration provides the foundation for evaluating treatment effectiveness and guiding iterative parameter adjustments across different stages. At the same time, geological factors, including fracture complexity and geomechanical responses, introduce significant uncertainty into fracture interpretation (Wang et al., 2024; Sun et al., 2025), often leading to non-unique solutions (Li et al., 2022a; Pei and Sepehrnoori, 2022; Ishibashi et al., 2023). These challenges highlight the necessity of developing diagnostic frameworks that not only capture fracture geometry and stimulated area using monitoring data but also incorporate geological constraints (Manjunath et al., 2023; Liu et al., 2024). Current diagnostic practices, however, remain fragmented, with pressure-based, microseismic, and fiber-optic methods often applied in isolation, lacking unified workflows for cross-validation. To reduce the interpretational non-uniqueness, it is essential to integrate mini-frac, main injection and post-fracturing pressure falloff analyses into a systematic pressure-based framework, enabling multi-scale diagnosis and verification, thereby establishing more reliable links between diagnostic outcomes and completion optimization.

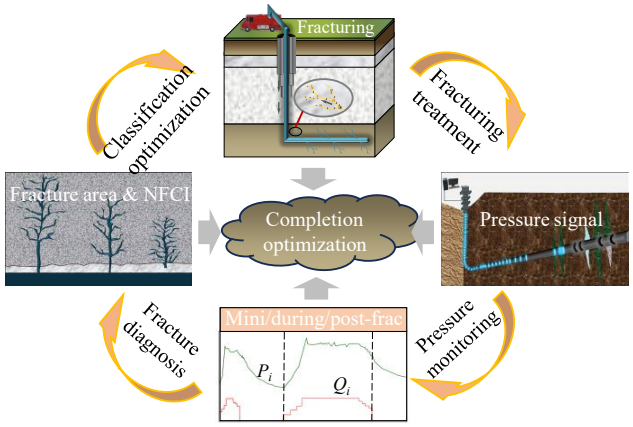

Fig. 1. Schematic framework of fracture diagnostics and optimization in unconventional reservoirs.

In order to address the above issues, this paper proposes a unified fracturing diagnostic framework based on fluid pressure signal interpretation and data mining. By incorporating pressure data from the mini-frac test, main fracturing, and post-fracturing pressure falloff, the framework enables the quantitative evaluation of fracture complexity and stimulated fracture area. The normalized fracture complexity index (NFCI) is defined from pressure responses to characterize dynamic fracture propagation, while the stimulated fracture area is obtained through pressure falloff analysis. Data mining is further employed to correlate these diagnostic indices with the fracturing completion parameters, thereby providing optimization strategies under various geological conditions. The proposed framework, validated on three horizontal coalbed methane wells from the Junggar Basin, provides a low-cost, efficient tool for diagnosing hydraulic fracturing performance and guiding unconventional completion optimization.

2. Methodology

This section presents a structured methodology for diagnosing post-fracturing behavior and optimizing stimulation parameters in unconventional reservoirs. Pressure curves, which are readily available during hydraulic fracturing operations, capture the integrated response of the wellbore, formation and fractures. The key to fracture diagnostics is to extract diagnostic features from these signals while minimizing the interference of rate-dependent friction. The proposed workflow incorporates pressure data from the mini-fracture, main injection, and falloff stages in an integrated manner. Fracture complexity is characterized by continuous wavelet transform (CWT) of corrected injection pressure signals, while fracture area is estimated from falloff pressure decline through inversion analysis. These results are then correlated with geological and operational parameters to identify the dominant controlling factors and provide guidance for data-driven stimulation optimization. To visually illustrate the overall idea, Fig. 1 presents a schematic framework of fracture diagnostics and

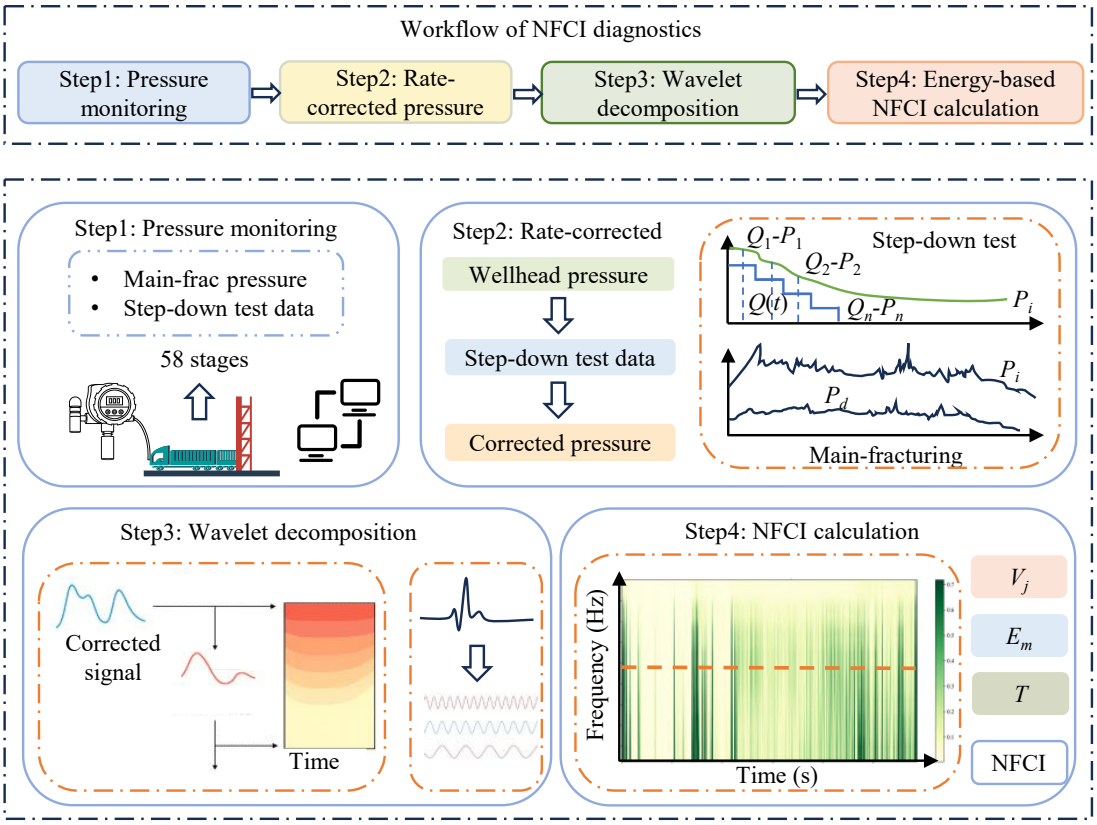

Fig. 2. Workflow of pressure-based NFCI diagnostics.

optimization in the development of unconventional resources.

2.1 Diagnosis of fracture complexity based on injection pressure

The diagnosis of fracture complexity is based on pressure and rate data during the main fracturing stage, in which the step-down test plays a critical role. During fracturing operations, wellhead pressure is jointly influenced by the injection rate, frictional losses, and the fracture propagation state. Variations in the injection rate can cause abrupt changes in frictional pressure, thereby introducing interference into fracture diagnostics. The step-down test is designed to establish a dynamic relationship between injection rate and system friction. Frictional losses are composed of wellbore friction, perforation friction, and near-wellbore friction. As shown in Eq. (1), the combined wellbore and perforation friction is typically modeled as a quadratic function of rate, while near-wellbore friction is represented as proportional to the square root of rate. By performing a step-wise reduction in rate, multiple stable pressure points under different flow conditions can be obtained. Fitting these data points to Eq. (1) yields the friction coefficients K_1 and K_2, which define the rate-dependent frictional behavior of the system (Mondal et al., 2021):

$$P(R) = K_1 Q^2 + K_2 Q^{0.5} \tag{1}$$

where $P(R)$ represents the rate-dependent frictional pressure, MPa; Q represents the injection rate, m^3/min; K_1 represents the quadratic coefficient representing wellbore and perforation friction, MPa·(min/m^3)^2; and K_2 represents the near-wellbore friction coefficient, MPa·(min/m^3)$^{0.5}$.

Once the friction coefficients are determined, the instantaneous pressure contribution attributed solely to fracture behavior can be calculated using Eq. (2) by subtracting the rate-induced frictional pressure from the measured wellhead pressure. This corrected pressure is denoted as P_d. Through this procedure, the interference caused by rate variations is effectively removed using data from the step-down test, allowing P_d to better represent the actual fracture propagation response (Mondal et al., 2021):

$$P_d(t) = P_i(t) - K_1 Q(t)^2 - K_2 Q(t)^{0.5} \tag{2}$$

where $P_i(t)$ represents the measured wellhead pressure at time t, MPa; $P_d(t)$ represents the corrected pressure excluding frictional losses, MPa; and $Q(t)$ is the instantaneous injection rate, m^3/min.

In order to capture dynamic features related to fracture propagation, the corrected pressure signal P_d is further processed using the CWT. As shown in Fig. 2, high-frequency components, particularly in the 0.3-0.5 Hz range, have been widely recognized as markers of transient fracture phenomena such as tip advancement, sudden branching and fracture interactions (Unal et al., 2019). These relationships have been validated through both numerical simulations and field observations (Hu et al., 2022).

In order to improve the characterization of such instabili-

ties, the NFCI is proposed. This index accounts for both the intensity and persistence of high-frequency pressure fluctuations while normalizing for the injection scale. Specifically, the CWT is used to compute the time-frequency energy distribution of P_d from which the average spectral energy in the 0.3-0.5 Hz band is extracted at each time step. A dynamic activation threshold is defined as 1.5 times the mean energy level over the entire injection period. In this study, the CWT is implemented using the Morlet mother wavelet (morl). The corrected pressure signal is uniformly resampled, and the analysis focuses on the 0.3-0.5 Hz frequency band, which is most sensitive to transient fracture activities.

The time intervals where the spectral energy exceeds this threshold are identified as high-frequency activation periods. Then, the cumulative energy exceeding the threshold within these intervals is integrated and normalized by the mean energy level and the total injected fluid volume, yielding the final NFCI value. In other words, the NFCI incorporates the intensity (spectral energy), persistence (activation duration), and scale effect (injection volume) of high-frequency pressure fluctuations, ensuring comparability across different stages and wells. This approach provides a more physically representative indicator of unstable fracture growth, enhancing sensitivity to both signal amplitude and duration. The full formulation is given in Eq. (3). Physically, NFCI reflects the degree to which a reservoir responds to injected energy through unstable fracture growth, including branching, tip advancement and fracture interactions, while highlighting the intrinsic dynamic sensitivity of the fracture system to stimulation:

$$N_f = \frac{1}{V_j}\int_0^T \left\{ \frac{E(t, f \in F)}{E_m} [I(E(t, f \in F) > \alpha E_m)] \right\} \mathrm{d}t \quad (3)$$

where N_f represents the NFCI, dimensionless; $E(t, f \in F)$ represents the spectral energy at time t within the frequency band F, MPa^2·s; E_m represents the mean spectral energy during injection, MPa^2·s; α represents the threshold multiplier, dimensionless, 1.5; I represents the indicator function for activation, dimensionless; V_j represents the total injected fluid volume, m^3; and T represents the total injection time of a single fracturing stage, s.

2.2 Diagnosis of fracture area based on pressure falloff analysis

The diagnosis of fracture area is carried out from the shut-in pressure falloff curve after hydraulic fracturing, which provides insights into fluid leak-off behavior and fracture geometry. Conventional G-function-based methods assume planar fractures and Carter-type leak-off during the entire shut-in period. However, in actual reservoirs, abnormal responses such as water hammer, wellbore storage, or early fracture closure often occur, causing deviations from the ideal assumption and leading to significant overestimation of the fracture area.

In order to improve robustness, an enhanced falloff analysis method is employed (Wei et al., 2024). The key step is the use of CWT to decompose the falloff signal and identify the nearly pure leak-off phase, in which the pressure decline is mainly controlled by leak-off with minimal interference from other effects. The CWT is expressed as (Wei et al., 2024):

$$W_f(a,b) = |a|^{-\frac{1}{2}} \int_R f(t)\psi\left(\frac{t-b}{a}\right)\mathrm{d}t \quad (4)$$

where W_f represents the coefficient of the wavelet function, MPa·s; $f(t)$ represents the analyzed signal (here: Corrected pressure signal P_d), MPa; ψ represents the Morlet mother wavelet; R represents the integration domain, dimensionless; a represents the expansion factor that can affect the shape of the wavelet, dimensionless; and b represents the translation factor that affects the phase of the wavelet, dimensionless.

Within this interval, the G-function derivative is used to link pressure decline with fracture area (Liu and Ehlig-Economides, 2019):

$$\frac{\mathrm{d}P}{\mathrm{d}G} = \frac{\pi C_L \sqrt{t_p}(A_m + A_n)}{2(c_m A_m + c_n A_n)} \quad (5)$$

where $\mathrm{d}P/\mathrm{d}G$ represents the derivative of pressure with respect to G-function time, MPa; C_L represents the leak-off coefficient, m/min$^{0.5}$; t_p represents the time from fracture initiation to pump shutdown, min; A_m and A_n represent the areas of main and secondary fractures, m^2; and c_m, c_n are their respective compliances, m/MPa.

In addition, the material balance relationship, which represents the balance of fracturing fluid volume, is expressed as (Liu and Ehlig-Economides, 2019; Wei et al., 2024):

$$V_p = c_m A_m (P_s - P_m) + c_n A_n (P_s - P_n) + 2 r_p C_L \sqrt{t_p + \Delta t}(A_m + A_n) g_0 \quad (6)$$

where V_p represents the equivalent injected volume per stag, m^3; P_s represents the instantaneous shut-in pressure, MPa; P_m and P_n represent the closure pressures of main and secondary fractures, MPa; r_p represents the ratio of leak-off height, dimensionless; Δt represents the leak-off correction time, min; and g_o is the G-function constant, dimensionless.

By solving Eqs. (5) and (6) simultaneously, the areas of main and secondary fractures can be determined. The mechanical parameters involved in these equations, such as fracture closure pressures and compliances, are typically obtained from mini-frac tests or laboratory rock mechanics experiments, in order to ensure that the inversion results have a reliable physical basis. More importantly, the main fracture area can be separated, which represents the wide fractures that are most likely to be propped. For clarity, in the following sections, the sum of A_n and A_m is collectively referred to as the stimulated fracture area, while A_m is denoted as the main fracture area. Compared with conventional methods, this approach improves the robustness of falloff interpretation by filtering out abnormal responses through CWT, making it a more practical parameter for evaluating fracturing effectiveness. The workflow of fracture area estimation from falloff analysis is illustrated in Fig. 3.

2.3 Correlation analysis and optimization of completion

In order to identify the dominant controls of fracture morphology and support data-driven stimulation optimization, a correlation analysis is performed between geological and

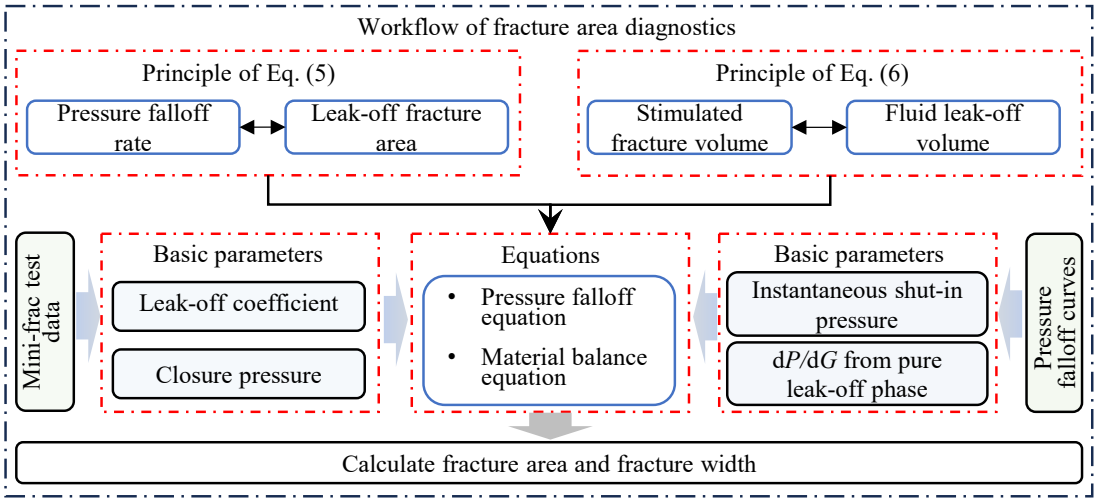

Fig. 3. Workflow of fracture area diagnostics from post-fracturing pressure falloff analysis.

Table 1. Classification of parameters used in the correlation analysis.

Geological	Engineering	Fracture evaluation results
Average mechanical specific energy	Total fluid volume	Stimulated fracture area
Variance in MSE	Sand ratio	Main fracture area
Breakdown pressure	Average injection rate	Average fracture width
Instantaneous shut-in pressure	Stage length	NFCI

engineering parameters and fracture diagnostics results. The objectives are twofold: First, to quantify the influence of both engineering and geological factors on fracture complexity and stimulated fracture area; second, to extract optimized parameter combinations or design recommendations for different geological settings, thereby providing guidance for stage-level optimization in future completions. A total of 12 variables are included in the analysis and grouped into three categories: Geological parameters, engineering design variables, and fracture response indicators, as illustrated in Table 1.

Several parameters in this analysis are not directly measurable but derived from multi-source field data. For example, mechanical specific energy (MSE) is employed as a composite indicator of rock strength and fracability, essentially reflecting the confining compressive strength of the rock. In this study, a corrected bottomhole mechanical specific energy is applied to account for drillstring friction, torque loss, compound rotary-motor drilling, and jet-assisted rock breaking. This corrected mechanical specific energy can more accurately reflect the actual rock-breaking energy at the bit and capture small-scale heterogeneity in formation strength along the lateral. Stage-level variance in MSE is further used to represent geological variability within individual stages, and its expression is (Hu et al., 2023b):

$$M_b = \frac{W_e}{A_b} + \frac{120\pi N_b T_b}{A_b V_c} + \frac{\eta \Delta P_b Q_b}{A_b V_c} \tag{7}$$

where M_b represents the corrected bottomhole mechanical specific energy, MPa; W_e represents the effective weight on bit, kN; A_b represents the bit area, m^2; N_b represents the corrected rotary speed, rev/min; T_b represents the corrected torque, KN·m; V_c represents the penetration rate, m/h; ΔP_b represents the pressure drop across the bit, MPa; Q_b represents the flow rate at the bit, m^3/min; and η represents the hydraulic efficiency factor, dimensionless.

In order to evaluate the relationships between inputs and outputs, Spearman rank correlation is employed to quantify the monotonic associations between geological/engineering parameters and fracture-response indicators. The Spearman coefficient is defined as the Pearson correlation of the rank variables, which does not require normal distribution assumptions and is therefore more robust under field data conditions (Dewinter et al., 2016):

$$\rho_s = \frac{\sum_{i=1}^{n} \left(R_{x,i} - \overline{R_x}\right)\left(R_{y,i} - \overline{R_y}\right)}{\sqrt{\sum_{i=1}^{n} \left(R_{x,i} - \overline{R_x}\right)^2} \sqrt{\sum_{i=1}^{n} \left(R_{y,i} - \overline{R_y}\right)^2}} \tag{8}$$

For tie-free data, an equivalent closed form is (Dewinter et al., 2016):

$$\rho_s = 1 - \frac{6\sum_{i=1}^{n} d_i^2}{n\left(n^2 - 1\right)}, \quad d_i = R_{x,i} - R_{y,i} \tag{9}$$

where ρ_s represents the Spearman rank correlation coefficient, dimensionless; n represents the sample size, $R_{x,i}$ represents the rank of the i-th observation of variable X, $R_{y,i}$ represents the rank of the i-th observation of variable Y, $\overline{R_x}$ represents

Table 2. Main fracturing parameters of wells A-C.

Well	Stages	Average stage length (m)	Average cluster spacing (m)	Clusters per stage	Fluid system	Injection rate (m^3/min)	Proppant intensity (m^3/m)
A	22	63.0	18.8	3-4	High-viscosity	20	2.6
B	21	42.5	20.7	2	High-viscosity	12	1.84
C	15	60.4	19.6	4	Variable-viscosity	20	3.9

the mean rank of variable X, $\overline{R_y}$ represents the mean rank of variable Y, and d_i is the difference in ranks of the i-th observation.

The resulting Spearman correlation matrix identifies key drivers with significant influence on the fracture complexity and stimulated fracture area under field data conditions (which need not be normally distributed). Furthermore, stages with favorable outcomes are statistically grouped based on fracture performance, allowing the extraction of optimized parameter ranges for given geological conditions. Building on these findings, geology-based classification is introduced in the next section to enable the application of stage-specific optimization strategies under varying geological conditions.

3. Results and analysis

This study presents a case study of 3 hydraulically fractured wells in a typical coalbed methane reservoir of the Junggar Basin, Xinjiang, China. A total of 58 fracturing stages were analyzed, covering varied geological settings and treatment designs. Pressure curve interpretation and fracture inversion were used to evaluate the fracture morphology, with representative stages examined in detail and a geology-based classification proposed for parameter recommendations.

3.1 Overview of the application wells

This study investigates three horizontal wells, referred to as Well A, Well B and Well C, that were completed with multi-stage hydraulic fracturing. The wells differ primarily in their stage/cluster configurations, fracturing fluid systems, injection schedules, and proppant intensities. A summary of the main operational parameters is provided in Table 2.

Wells A, B and C were completed with distinct stage/cluster designs and fluid programs. Well A comprised 22 stages with 3-4 clusters per stage; the average stage length and mean cluster spacing were 63.0 m and 18.8 m, respectively. A high-viscosity fluid system was pumped at 20 m^3/min, and the proppant intensity was 2.6 m^3/m. Well B comprised 21 stages with 2 clusters per stage; the average stage length was 42.5 m and the mean cluster spacing was 20.7 m; a high-viscosity fluid system was used at 12 m^3/min, and the proppant intensity was 1.84 m^3/m. Well C comprised 15 stages with 4 clusters per stage; the average stage length and mean cluster spacing were 60.4 m and 19.6 m; a variable-viscosity fluid system was pumped at 20 m^3/min, and the proppant intensity was 3.9 m^3/m.

These operational contrasts, particularly in fluid type, injection rate and proppant intensity, provide a sound basis for evaluating fracture geometry and treatment effectiveness in the following sections.

3.2 Fracture parameter interpretation

On the basis of pressure curve interpretation, the fracture morphology and stimulation responses were quantified for three hydraulically fractured wells. Eight key indicators were derived for each of the 58 stages, including stimulated fracture area, main fracture area, average fracture width, NFCI, mechanical specific energy, variance of mechanical specific energy per stage, total fluid volume, and sand ratio (Fig. 4). Well A showed stimulated fracture areas ranging from 1.9×10^5 to 6.4×10^5 m^2 with an average of 3.8×10^5 m^2, and main fracture areas from 8.1×10^4 to 2.6×10^5 m^2 with an average of 1.5×10^5 m^2. The average fracture width ranged between 0.9 and 4.0 mm, while NFCI values varied between 0.044 and 0.118. Well B had stimulated fracture areas of 7.7×10^4-6.1×10^5 m^2 and main fracture areas of 4.1×10^4-3.5×10^5 m^2. The fracture width was in the range of 0.6-2.8 mm, and NFCI values were 0.038-0.110. Well C exhibited stimulated fracture areas of 1.1×10^5-3.1×10^5 m^2 and main fracture areas of 7.1×10^4-1.4×10^5 m^2. The fracture width ranged from 0.23 to 3.5 mm, while NFCI values were between 0.049 and 0.135.

In terms of average diagnostic parameters, the stimulated fracture area followed the order A > B > C, while the main fracture area followed B > A > C. Average fracture width was highest in Well A, with Wells B and C showing similar but smaller values. NFCI was ranked C > A > B, indicating that Well C experienced the most complex fracture networks, whereas Well B remained the simplest. These trends are consistent with the completion designs: The lower injection rate in Well B limited fracture width but favored stable planar growth, the higher injection rate and variable-viscosity system in Well C promoted branching and complexity, while Well A represents an intermediate case with wider fractures but moderate proppant effectiveness.

In order to illustrate the diagnostic workflow and underlying fracture propagation mechanisms, three representative stages were selected: A high-complexity stage (Case 1, Well C-Stage 2), a stage with the best proppant effectiveness (Case 2, Well B-Stage 14), and a wide-fracture stage (Case 3, Well A-Stage 20). These stages were chosen to cover the extreme and typical responses observed in the dataset, thereby providing the most illustrative examples of contrasting fracture behaviors. Each example integrates the corrected pressure response, CWT high-frequency energy distribution, and falloff

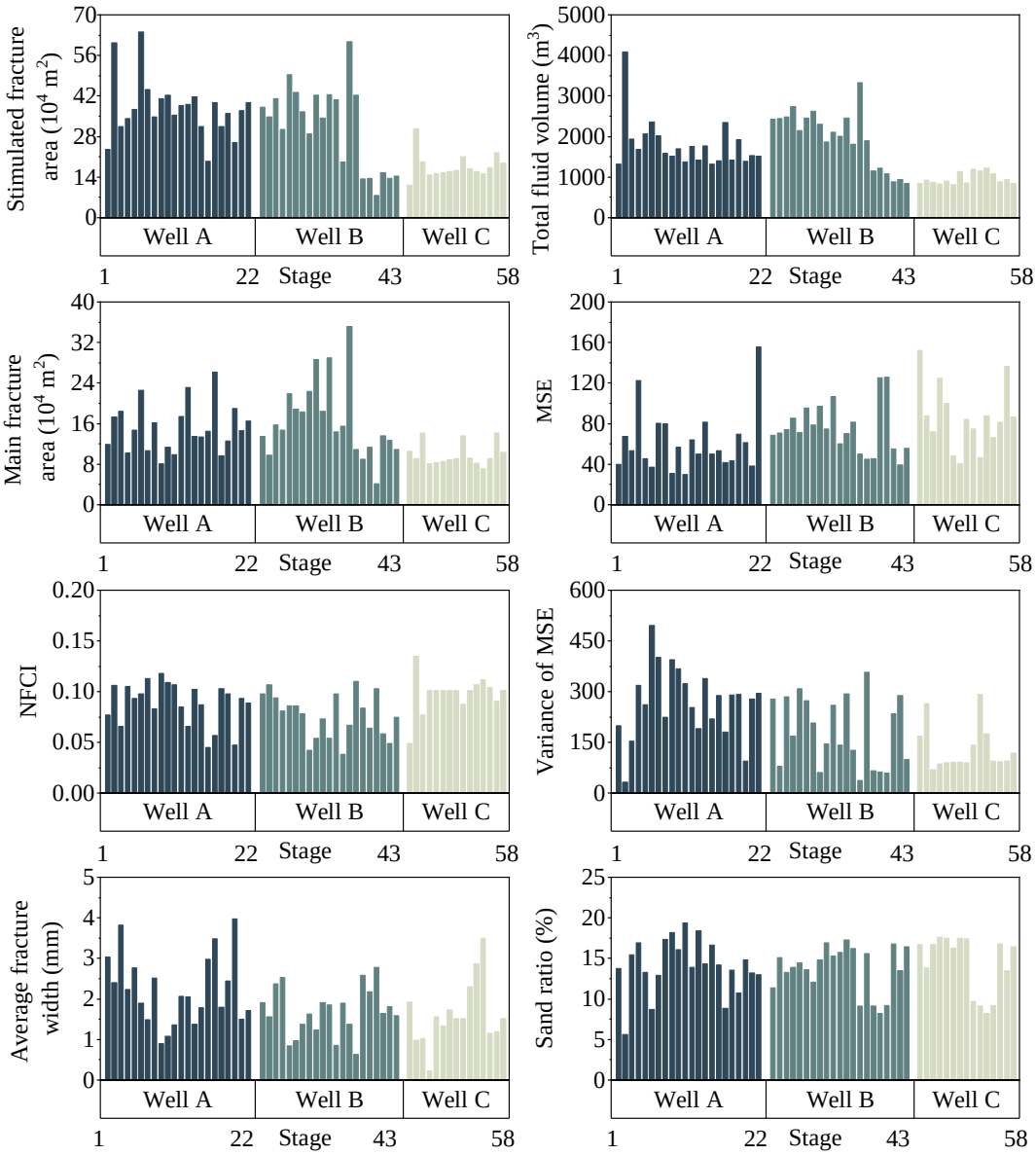

Fig. 4. Comparison of fracture morphology parameters, stimulation inputs, and MSE characteristics across 58 fracturing stages from wells A, B and C.

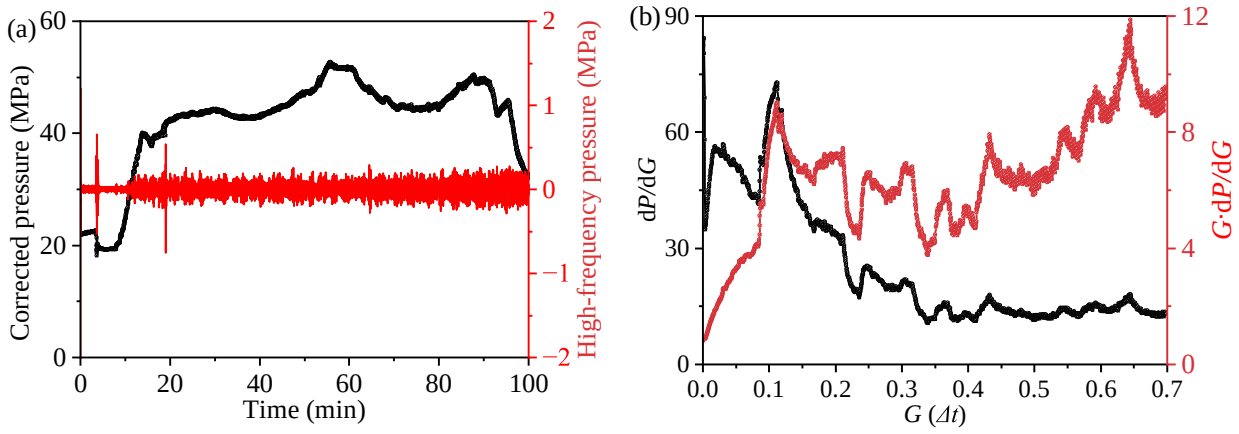

Fig. 5. Pressure analysis of Case 1 during and after fracturing: (a) Corrected and high-frequency pressures and (b) G-function characteristic curves.

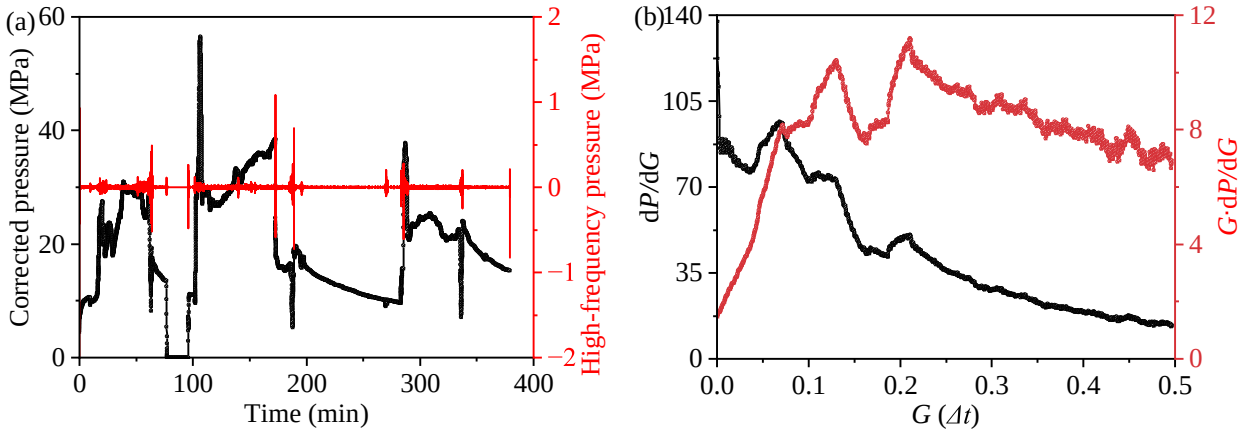

Fig. 6. Pressure analysis of Case 2 during and after fracturing: (a) Corrected and high-frequency pressures and (b) G-function characteristic curves.

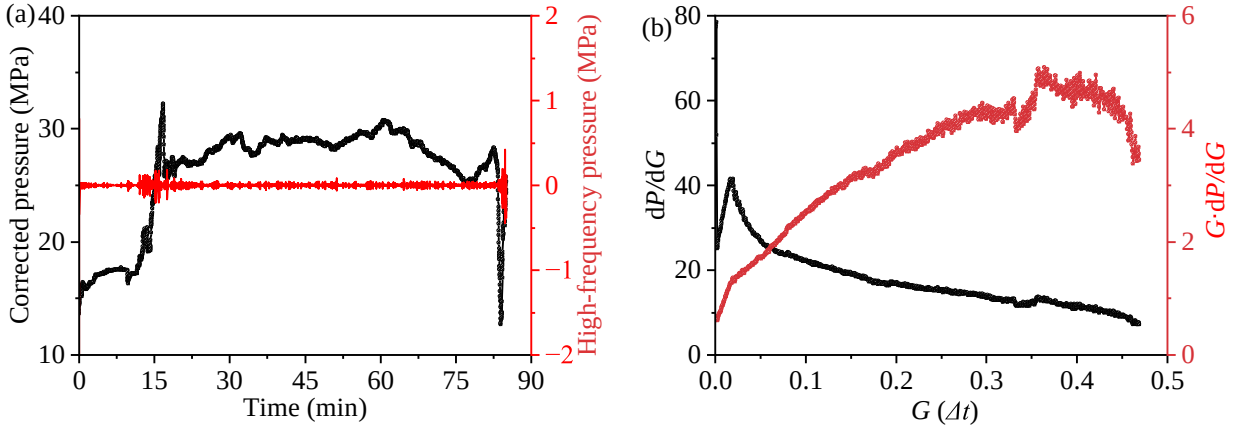

Fig. 7. Pressure analysis of Case 3 during and after fracturing: (a) Corrected and high-frequency pressures and (b) G-function characteristic curves.

analysis. (Figs. 5-7).

Case 1: High-complexity stage. The corrected pressure exhibits rapid oscillations, while the CWT spectrum reveals strong bursts of high-frequency energy, indicative of secondary microfracture activation and frequent branching. The falloff response departs from a linear trend and the G-function derivative curve shows multiple inflection points, consistent with the non-uniform fracture closure behavior (Fig. 5). The inversion results indicate a stimulated fracture area of 305,876 m^2, a main fracture area of 90,957 m^2, and an average fracture width of 0.98 mm, with a NFCI of 0.134. Mechanistically, this stage is dominated by a branched fracture network with fine-scale apertures, providing complex connectivity.

Case 2: Best proppant effectiveness. The CWT spectrum exhibits distinct fluctuations, reflecting multiple fracture initiations. The G-function superposed derivative shows two closures, which is simpler in form compared with Case 1, representing a moderately complex fracture network (Fig. 6). Inversion confirmed that this stage achieved the largest stimulated and main fracture areas among the three cases: A stimulated fracture area of 607,194 m^2, main fracture area of 351,660 m^2, an average fracture width of 1.37 mm, and a NFCI of 0.067. Overall, the fracture system at this stage is relatively large in scale and structurally stable, providing favorable conditions for uniform proppant placement, thereby achieving the most effective proppant utilization among the three cases.

Case 3: Wide-fracture stage. The corrected pressure curve remains relatively stable, and the CWT spectrum is dominated by low-frequency components with weak high-frequency signals, indicating a relatively simple fracture morphology dominated by planar fractures with limited branching. The falloff response is smooth and the G-function superposed derivative exhibits a simple form, reflecting a single planar-fracture morphology (Fig. 7). The inversion results show a stimulated fracture area of 260,001 m^2, a main fracture area of 189,411 m^2, an average fracture width of 3.96 mm, and a NFCI of 0.047. Overall, this stage is characterized by a more regular and large-scale planar fracture structure, with little evidence of complex branching. Such morphology ensures a wide fracture

aperture but also reflects limited fracture-network complexity.

3.3 Validation of the proposed method using FDEM

In order to validate the reliability of pressure-derived fracture parameters, three-dimensional fracture propagation was simulated using the finite-discrete element method (FDEM). A stratified model of 120 m × 30 m × 30 m was constructed, consisting of roof, coal seam, interlayer, and floor (Fig. 8). Certain geomechanical parameters including elastic modulus, Poisson's ratio, tensile strength, and fracture energies were assigned to each layer based on core and log data (Table 3).

According to the inversion results, Well B had the largest average main fracture areas (1.7×10^5 m^2), Well C showed the highest NFCI (0.098) and the narrowest average fracture width (1.6 mm), while Well A displayed intermediate values with wider apertures (2.2 mm) but moderately higher complexity (0.088). Fig. 9 statistically compares the pressure-derived parameters among the three wells.

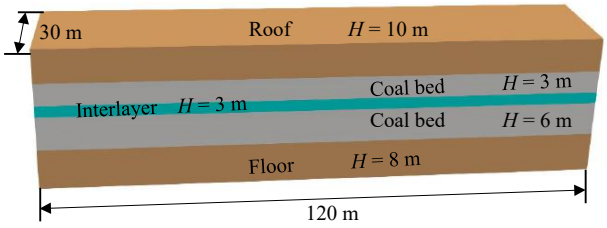

Fig. 8. Stratigraphic model used for fracture simulation, consisting of roof, coal beds, interlayer, and floor.

Table 3. Basic geomechanical parameters of the formation.

Layer	Elastic modulus (GPa)	Poisson's ratio	Tensile strength (MPa)	Mode I fracture energy (N/m)	Mode II fracture energy (N/m)	Cohesion (MPa)
Roof	16	0.2	2.5	140	1,400	20
Coal	2.5	0.32	1	60	600	3.4
Interlayer	12	0.25	2	120	1,200	12
Floor	16	0.2	2.5	140	1,400	20

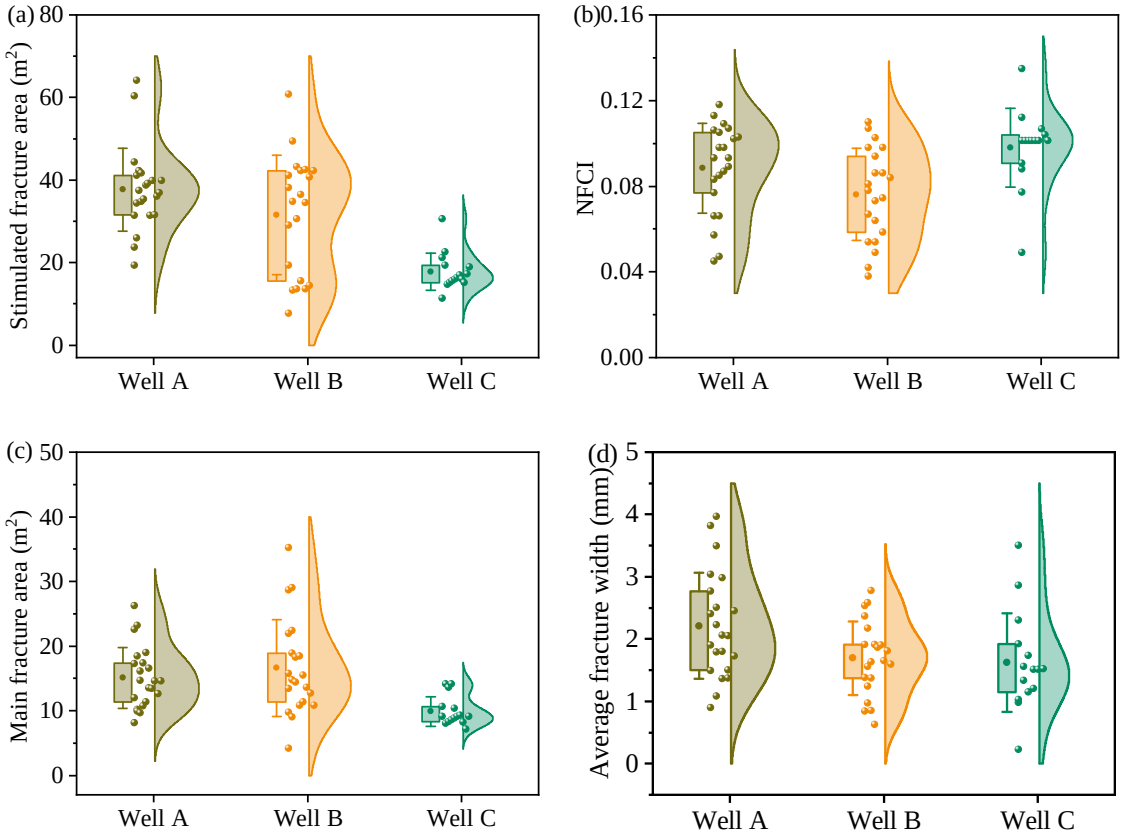

Fig. 9. Statistical comparison of fracture evaluation results for Wells A, B and C: (a) Stimulated fracture area, (b) NFCI, (c) main fracture area, and (d) average fracture width.

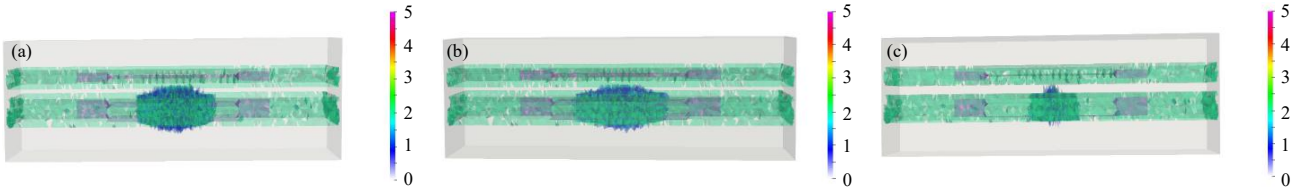

Fig. 10. Simulated fracture propagation patterns for Wells (a) A, (b) B, and (c) C under typical pumping conditions.

Table 4. Summary of FDEM-simulated fracture morphology statistics.

Well	Fracturing fluid type	Fracture morphology	Tensile/Shear/Mixed fracture ratio (%)
A	High-viscosity	Combination of main and branch fractures	19.6/70/10.4
B	High-viscosity	Dominated by main fractures	12.5/76/11.5
C	Variable-viscosity	Dominated by branch fractures	20.5/68/11.5

Subsequently, FDEM simulations were conducted under representative pumping conditions. The simulated fracture propagation patterns for the three wells are shown in Fig. 10. Well B exhibited predominantly planar fractures with the largest average stimulated fracture area, consistent with its large main fracture area from inversion. In contrast, Well C developed more branched fractures with a higher proportion of tensile failures, in line with its higher NFCI values. Well A showed intermediate characteristics with a mixture of main and branched fractures. To further quantify the fracture characteristics, fracture morphology statistics were derived from the FDEM simulations (Table 4). Well A developed a combination of main and branch fractures, with tensile/shear/mixed failure ratios of 19.6%/70%/10.4%, consistent with its moderate NFCI and wider apertures. Well B was dominated by planar fractures, with ratios of 12.5%/76%/11.5%, in agreement with its large main fracture area and lowest NFCI. Well C produced branched fracture networks with the highest tensile proportion (20.5%/68%/11.5%), consistent with its highest NFCI and narrowest widths.

Overall, the FDEM simulations reproduced the same inter-well trends observed from pressure-based inversion: Wells with greater main fracture areas corresponded to planar fractures, while wells with higher NFCI were associated with more branched fractures and limited conductivity. This consistency demonstrates that the diagnostic framework is not only mathematically distinguishable but also mechanically plausible under realistic geological constraints, thereby enhancing the reliability of the proposed methodology.

3.4 Controlling factors and parameter recommendations

In order to identify the key geological and engineering factors controlling fracture morphology, parameters of drilling, logging and fracturing operation were collected from three wells, and a correlation analysis was conducted using the fracture inversion results from 58 stages. In this study, Spearman's rank correlation coefficients were employed to evaluate the relationships between fracture parameters and geological/engineering parameters. The Spearman correlation matrix highlights the monotonic relationships between fracture diagnostics and geological/operational parameters, with significant correlations indicated by asterisks (Figs. 11 and 12). For clarity, all parameters in the figure are denoted by the abbreviations defined in Table 1. The correlation analysis indicates that larger fluid volumes are significantly associated with greater stimulated and main fracture areas, confirming that sufficient fluid supply is critical for maximizing stimulated reservoir volume. In contrast, excessively high average injection rates tend to increase fracture complexity and reduce overall fracture width, suggesting that overly aggressive pumping may promote narrower and more irregular fractures.

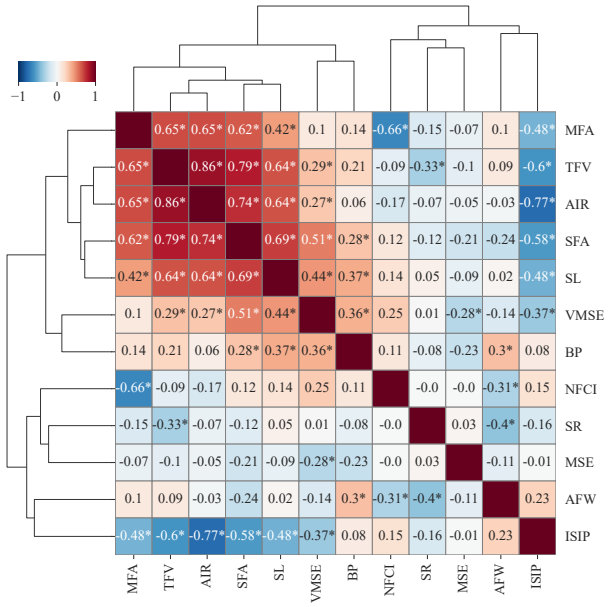

Fig. 11. Spearman's correlation matrix showing monotonic relationships. $p < 0.05$ is marked with asterisks.

During hydraulic fracturing, the variation in fracture area with the injected fluid volume is an important aspect to be considered. The stimulated fracture area exhibits a strong positive correlation with the total fluid volume, indicating

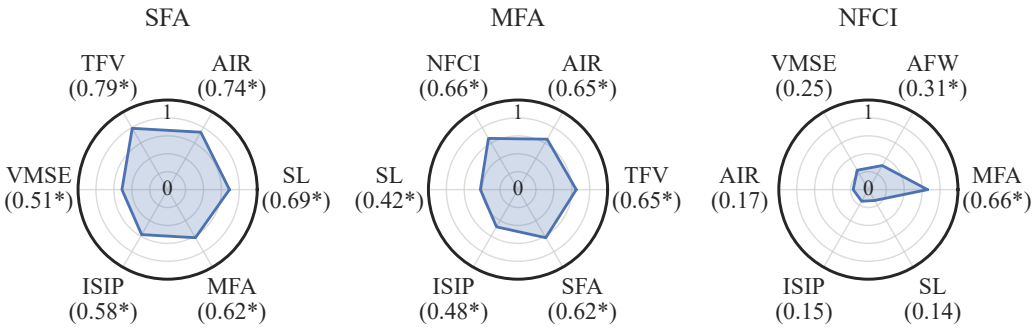

Fig. 12. Radar charts of Spearman's correlations between stimulated fracture area (SFA), main fracture area (MFA), and NFCI. The radar chart displays the abbreviations of the respective parameters.

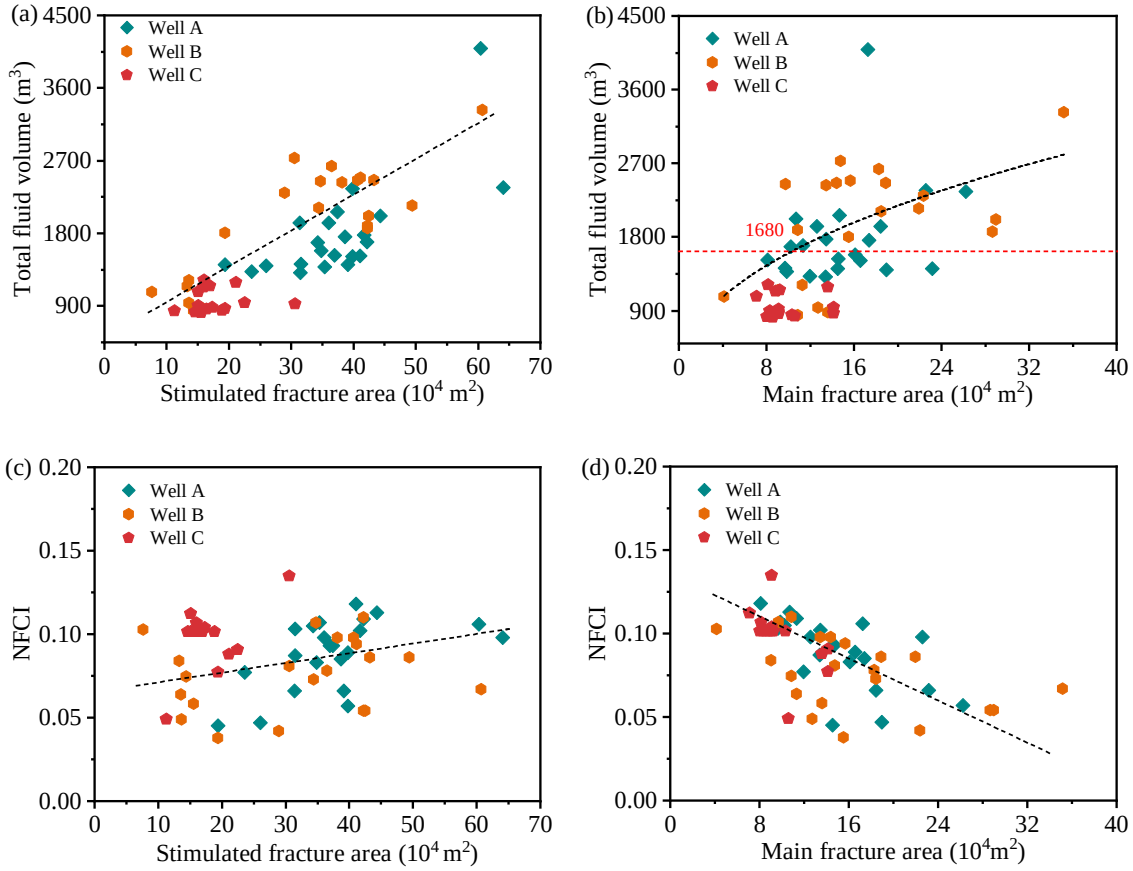

Fig. 13. Relationships between fracture area, fluid volume, and NFCI. (a) Stimulated fracture area vs total fluid volume, (b) main fracture area vs total fluid volume, (c) stimulated fracture area vs NFCI, and (d) main fracture area vs NFCI.

that greater fluid input generally promotes fracture extension in the formation (Fig. 13(a)). In contrast, the relationship between main fracture area and total fluid volume follows a nonlinear trend, showing a diminishing increase with fluid volume (Fig. 13(b)). A clear inflection point appears at approximately 1,680 m^3, beyond which additional fluid contributes little to further growth of the main fracture area. This suggests that although higher fluid volumes facilitate fracture creation, proppant placement efficiency may decline beyond this threshold. When analyzing the link between fracture area and fracture complexity, different trends are observed. The stimulated fracture area shows a weak positive correlation with the NFCI (Fig. 13(a)), implying that larger fracture networks can provide more branching and intersections. However, the main fracture area exhibits a clear negative correlation with fracture complexity (Fig. 13(d)). This reflects a fundamental fracture propagation mechanism: As fractures become more complex with increased branching and secondary fracture development, the continuity and openness of proppant-supported channels decrease, reducing the effective main fracture area. This highlights the trade-off between fracture complexity and proppant effectiveness, which is critical for balancing fracture

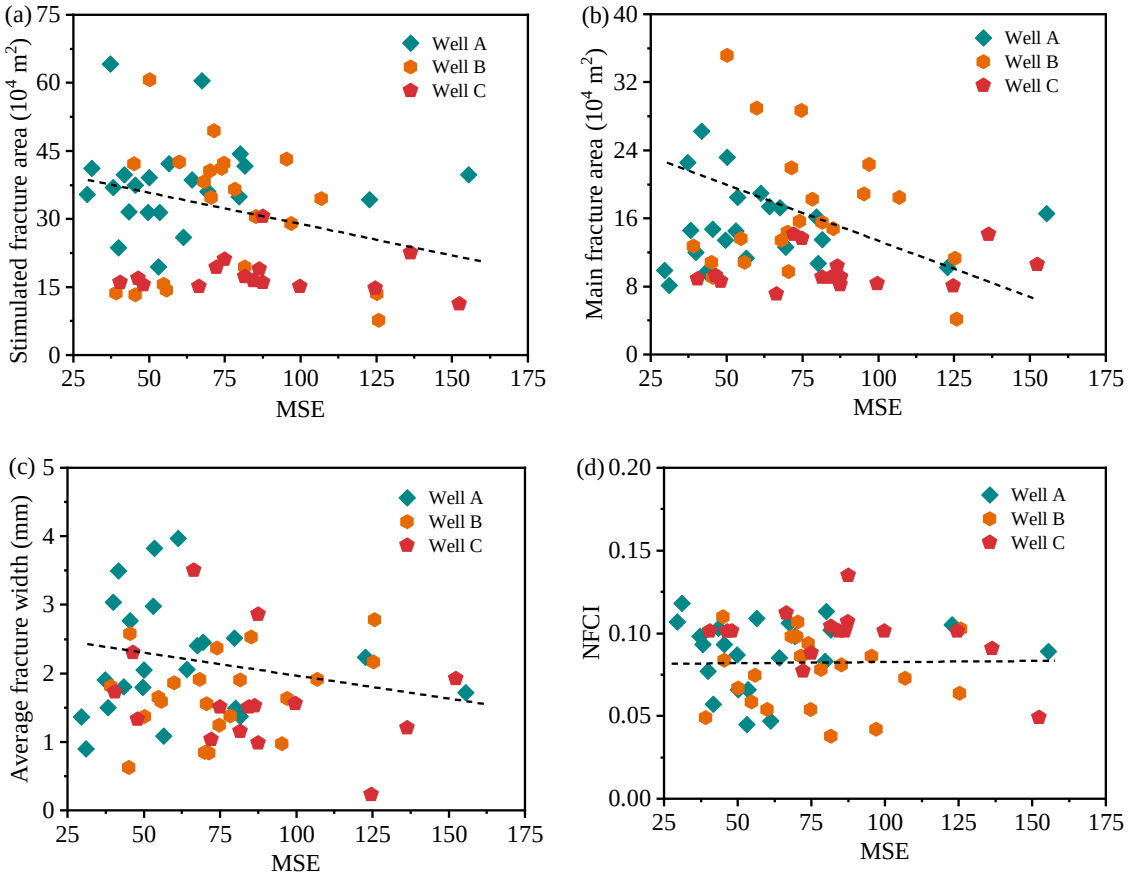

Fig. 14. Relationships between mechanical specific energy and fracture parameters: (a) Stimulated fracture area, (b) main fracture area, (c) average fracture width, and (d) NFCI.

conductivity and stimulated reservoir volume.

The analysis was further extended beyond operational parameters to incorporate geological conditions. The absolute value of MSE can be used to characterize the mechanical strength of the rock in the fractured interval. The MSE exhibits varying relationships with the fracture morphology parameters (Fig. 14). Both the stimulated fracture area and the main fracture area show an overall decreasing tendency with increasing MSE, although the scatter is considerable, suggesting that lower MSE generally favors larger fracture dimensions. The average fracture width does not display a strong correlation with MSE, while several high-MSE points correspond to wider fractures, implying that fracture apertures may increase under certain high-MSE conditions. The NFCI remains relatively scattered with only a slight decreasing trend as MSE increases, indicating that fracture complexity is not strongly sensitive to MSE. These results suggest that while MSE provides useful information about the fracture propagation efficiency, its control on specific fracture attributes is subject to large variability, and additional geological and operational factors must also be considered.

The variance in MSE along the length of the fracturing stage represents the heterogeneity of the formation. Likewise, the variance in mechanical specific energy exhibits meaningful relationships with fracture morphology (Fig. 15): A higher variance in mechanical specific energy corresponds to smaller main fracture area, indicating that unstable energy conditions are unfavorable for large-scale fracture propagation. Similarly, the average fracture width shows a decreasing trend with increasing mechanical specific energy variance, suggesting that unstable energy input suppresses the formation of wide fractures. In contrast, the NFCI increases with a larger mechanical specific energy variance, implying that fluctuations in energy conditions tend to promote irregular fracture propagation paths and enhance fracture complexity. These results highlight that apart from the absolute value of mechanical specific energy, its stability also plays a critical role in shaping fracture geometry. Building on these findings, mechanical specific energy was further applied as a practical criterion to classify fracturing stages and derive parameter recommendations. In this dataset, the midpoint of the mechanical specific energy values across the 58 analyzed stages is approximately 70, which provides a natural separation of the data. On this basis, MSE = 70 was adopted as a geological boundary to recommend optimized operational strategies for two different geological conditions (Table 5).

In low-MSE intervals, treatment parameters should emphasize fracture width enlargement while maintaining network connectivity. The recommended strategies include the use of higher-viscosity fluids, controlled pumping schedules to

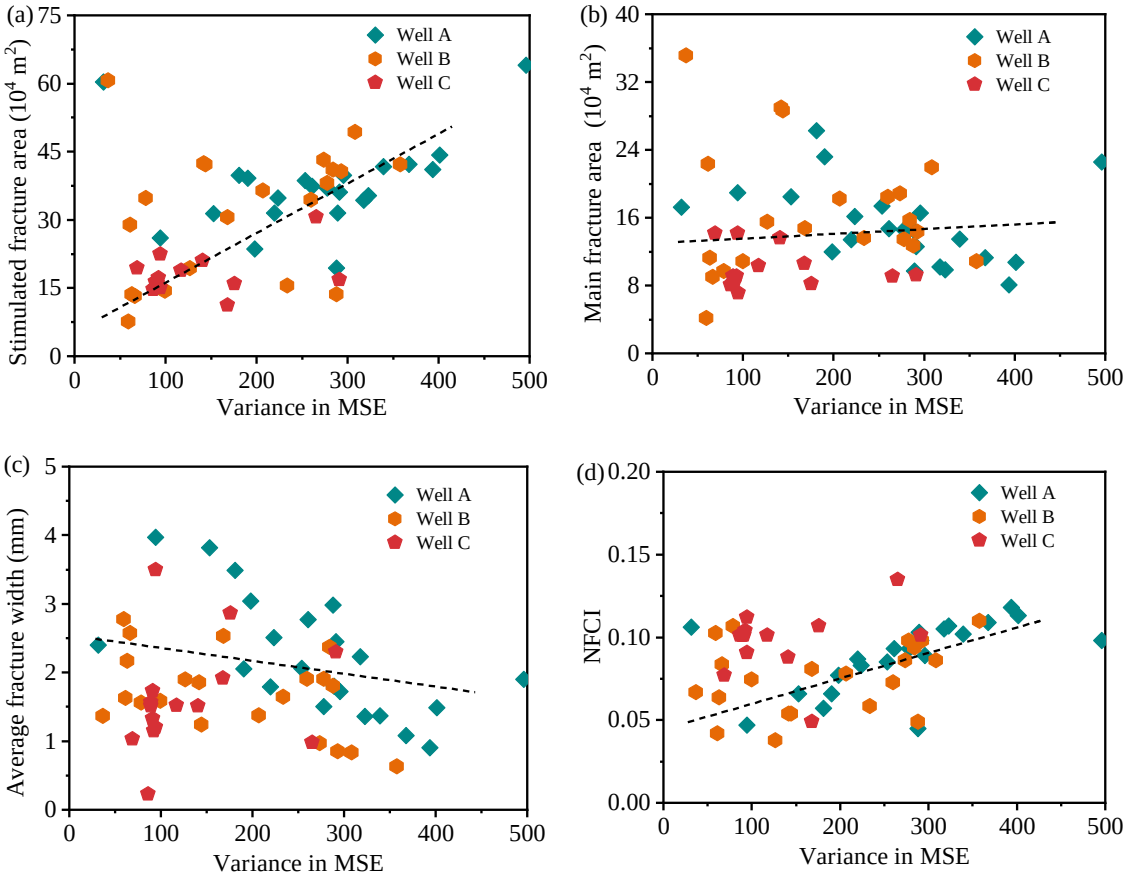

Fig. 15. Relationships between the variance of mechanical specific energy and fracture parameters: (a) Stimulated fracture area, (b) main fracture area, (c) average fracture width, and (d) NFCI.

Table 5. Parameter recommendations according to the MSE-based classification.

MSE class	Recommended strategy	Parameter adjustments
Low MSE (< 70)	Enhance width while maintaining complexity and area	High-viscosity fluids; controlled rate schedule; early introduction of medium-to-large mesh proppant; moderate tail-in increment (+15%-20%)
High MSE (≥ 70)	Promote complexity while maintaining conductivity	Slickwater or low-viscosity fluids; pumping rate +10%; +1 cluster or spacing -10%; diversion with 2-3 slugs; delayed introduction of heavy proppant

reduce near-wellbore tortuosity, early introduction of medium-to-large mesh proppant, and moderate tail-in proppant increment (+15%-20%). Meanwhile, in high-MSE intervals, treatment parameters should focus on promoting fracture complexity without compromising aperture. The recommended strategies include the use of slickwater or low-viscosity fluids, a 10%-15% increase in pumping rate, tighter stage spacing or additional clusters, diversion with 2-3 slugs per stage, delayed introduction of heavy proppant, and modest tail-sand increment (+10%). Thus, the geological conditions can be systematically linked with engineering optimization through stage classification.

4. Discussion

4.1 Practical advantages of the proposed method

The method proposed in this study demonstrates practical advantages owing to the integration of injection- and falloff-based diagnostics into a unified framework. Specifically, injection-derived NFCI captures fracture complexity in near real time, while falloff analysis provides estimates of fracture area. Applied together, the two phases yield complementary insights and converge on consistent interpretations. In Case 1 (Well C, Stage 2), strong oscillations in the injection spectrum produced a high NFCI (0.134), and the falloff-derived G-function curve displayed multiple closure behavior, both indicating branched fractures. In contrast, Case 3 (Well A, Stage 20) exhibited relatively smoother injection responses

Table 6. Comparison of the proposed framework with representative diagnostic methods.

Methods	Main outputs	Advantages	Limitations
Proposed framework	Fracture complexity; stimulated fracture area;	Low cost; Real-time complexity analysis	Dependent on pressure signal quality
G-function	Closure pressure; qualitative complexity	Mature and low-cost method	Post-treatment only
Water-hammer	Perforation efficiency; near-wellbore tortuosity	Effective for near-wellbore	Lacks far-field fracture information
Microseismic/Fiber/ Electromagnetic	Fracture extent; stimulated reservoir volume	Spatial mapping of fracture network	High cost and complex logistics

with a low NFCI (0.047), while the falloff analysis confirmed wide planar fractures, with a main fracture area of 189,411 m^2. These examples illustrate that fracture complexity and geometry can be jointly constrained by combining injection and falloff diagnostics, thereby reducing interpretational non-uniqueness.

Beyond the complementary constraints from main-frac and post-fracturing pressure falloff diagnostics, the reliability of this framework was independently validated through three-dimensional finite-discrete element method simulations. The simulated fracture morphologies reproduced the same inter-well trends inferred from pressure inversion: Well B developed predominantly planar fractures with the largest main fracture area, Well C generated branched networks with the highest NFCI and narrowest widths, and Well A exhibited intermediate behavior with wider apertures. These consistencies demonstrate that the pressure-derived NFCI and fracture area are not only mathematically consistent but also mechanically plausible under realistic geological constraints, thereby validating the robustness of the proposed method.

This framework is further contextualized among existing diagnostic methods (Maxwell, 2014; Wu et al., 2021; Anikiev et al., 2023; You et al., 2025). By contrast, the integrated pressure-based approach derives NFCI and fracture area directly from routine wellhead data without additional hardware, enabling the joint evaluation of injection and falloff phases and timely stage-by-stage feedback for multi-stage fracturing. Nonetheless, NFCI and fracture area are best suited for relative comparisons within the same reservoir and fluid system, while cross-reservoir applications require recalibration to local geological and operational conditions (Table 6).

4.2 Balance between complexity and main fracture area

The correlation results provide quantitative evidence of the trade-off between fracture complexity and the main fracture area. While complexity enhances the reservoir contact by promoting branching and lateral extension, effective fracture conductivity and production potential rely on maintaining a sufficient main fracture area to sustain fluid transport. Thus, the trade-off essentially reflects the competition between creating complex fracture networks and preserving continuous proppant-supported channels. Lower mechanical specific energy values are associated with larger stimulated fracture areas and higher complexity indices but smaller main fracture areas (Figs. 13-15). This indicates that under low-MSE conditions, fracture propagation tends to generate extensive branched networks, which increase stimulated reservoir volume but reduce the continuity of proppant-supported fractures. In contrast, higher MSE values correspond to lower complexity indices but larger main fracture areas, reflecting the dominance of more planar fractures that provide stable proppant placement and sustained conductivity, albeit with reduced reservoir coverage.

The above duality highlights a fundamental design challenge: Maximizing reservoir contact through complexity while avoiding the loss of effective main fracture area. Our correlation analysis further demonstrated that the complexity index is negatively correlated with the main fracture area, quantitatively confirming this competition. These findings suggest that neither fracture complexity nor main fracture area alone determines fracturing effectiveness; instead, a balance between the two must be sought to optimize stimulation outcomes. From a design perspective, this trade-off implies that stimulation strategies should pursue sufficient complexity to enhance reservoir contact, while they should simultaneously ensure adequate main fracture area to maintain conductivity and long-term production.

4.3 Geology-based classification for fracturing optimization

Our correlation analysis demonstrated that fracture morphology systematically varies with geological conditions. Intervals with favorable conditions for branching tend to develop extensive and complex networks but are constrained by smaller apertures, whereas intervals with more resistant formations tend to generate fewer but wider planar fractures with reduced complexity. This contrast reflects two competing regimes of fracture propagation, fundamentally governed by rock strength, stress state, and natural fabric.

Building on this principle, the geological characteristics provide a practical basis for classifying fracturing stages and tailoring design strategies. In intervals prone to high complexity, the priority is to enlarge fracture width while preserving network connectivity. The recommended approaches include:

(i) Using higher-viscosity or hybrid fluids to enlarge aperture;

(ii) Applying moderated injection schedules to reduce premature branching;
(iii) Lowering cluster density to concentrate energy;
(iv) increasing tail-in proppant loading to support branched geometries.

In more resistant intervals, the objective is to enhance complexity and reservoir contact without compromising aperture. The prevalent strategies include:

(i) Employing slickwater or low-viscosity fluids to stimulate secondary fractures;
(ii) Rraising pumping rates to increase dynamic energy;
(iii) Reducing stage spacing or adding perforation clusters;
(iv) Applying controlled diversion to activate additional pathways.

Looking forward, expanding the database to include multi-well and multi-reservoir information will allow the application of big-data and machine-learning approaches, further refining geology-based classification. Moreover, the proposed NFCI metric can be extended to real-time calculation, enabling the continuous assessment of fracture complexity during operations and supporting the real-time optimization of stimulation parameters.

5. Conclusions

This paper proposes an integrated pressure-based diagnostic framework that links fracture diagnostics with stimulation design. After applying this framework to 58 fracturing stages from three horizontal coalbed methane wells in the Junggar Basin, the main findings are as follows:

1) The stimulated fracture area per stage is primarily governed by the injected fluid volume and average injection rate, whereas the main fracture area and NFCI are significantly affected by the injection rate and geological factors represented by mechanical specific energy.
2) A significant negative correlation exists between the main fracture area and NFCI, indicating that fracturing parameter optimization must balance fracture complexity with the main fracture area.
3) Fracturing stages with greater MSE variance and lower average MSE are associated with the development of more complex fracture networks, whereas stages with smaller variance and higher MSE tend to produce simpler fracture geometries.
4) Fracturing parameter optimization in fracturing design should take stage-specific geological conditions into consideration.

Acknowledgements

The authors acknowledge the financial support provided by the National Natural Science Foundation of China (No. 52421002).

Conflict of interest

The authors declare no competing interest.

References

Afagwu, C., Mahmoud, M., Alafnan, S., et al. Multiscale storage and transport modeling in unconventional shale gas: A review. Journal of Petroleum Science and Engineering, 2022, 208: 109518.

Akbari, A., Karami, A., Kazemzadeh, Y., et al. Evaluation of hydraulic fracturing using machine learning. Scientific Reports, 2025, 15(1): 26926.

Anikiev, D., Birnie, C., Waheed, U., et al. Machine learning in microseismic monitoring. Earth-Science Reviews, 2023, 239: 104371.

Childers, D., Wu, X. Fracture diagnostic technologies with process workflow for implementation. Journal of Petroleum Science and Engineering, 2022, 208: 109778.

Cui, Q., Zhao, Y., Zhang, L., et al. A semianalytical model of fractured horizontal well with hydraulic fracture network in shale gas reservoir for pressure transient analysis. Advances in Geo-Energy Research, 2023, 8(3): 193-205.

Dewinter, J. C., Gosling, S. D., Potter, J. Comparing the Pearson and Spearman correlation coefficients across distributions and sample sizes: A tutorial using simulations and empirical data. Psychological Methods, 2016, 21(3): 273-290.

Ekechukwu, G. K., Sharma, J. Well-scale demonstration of distributed pressure sensing using fiber-optic DAS and DTS. Scientific Reports, 2021, 11(1): 12505.

Eltaleb, I., Soliman, M. Y., Ali, S. F., et al. Estimation of permeability from pump-in/flowback tests: An after-closure analysis approach. Fuel, 2025, 381: 133020.

Eyinla, D., Henderson, S. K., Emadi, H., et al. Optimization of hydraulic fracture monitoring approach: A perspective on integrated fiber optics and sonic tools. Geoenergy Science and Engineering, 2023, 231: 212441.

Hazlett, R., Farooq, U., Babu, D. A. A complement to decline curve analysis. SPE Journal, 2021, 26(4): 2468-2478.

Hu, X., Huang, G., Zhou, F., et al. Pressure response using wavelet analysis in the process of hydraulic fracturing: Numerical simulation and field case. Journal of Petroleum Science and Engineering, 2022, 217: 110837.

Hu, X., Tu, Z., Zhou, F., et al. A hydraulic fracture geometry inversion model based on distributed-acoustic-sensing data. SPE Journal, 2023a, 28(3): 1560-1576.

Hu, S., Sheng, M., Shi, S., et al. Optimization of fracturing stages/clusters in horizontal well based on unsupervised clustering of bottomhole mechanical specific energy on the bit. Natural Gas Industry B, 2023b, 10(6): 583-590.

Hudson, T., Baird, A., Kendall, J., et al. Distributed acoustic sensing (DAS) for natural microseismicity studies: A case study from Antarctica. Journal of Geophysical Research: Solid Earth, 2021, 126(7): e2020JB02149.

Ishibashi, T., Asanuma, H., Mukuhira, Y., et al. Laboratory hydraulic shearing of granitic fractures with surface roughness under stress states of EGS: Permeability changes and energy balance. International Journal of Rock Mechanics

and Mining Sciences, 2023, 170: 105512.

Lei, Q., Weng, D., Guan, B., et al. A novel approach of tight oil reservoirs stimulation based on fracture controlling optimization and design. Petroleum Exploration and Development, 2020, 47(3): 632-641.

Li, M., Magsipoc, E., Abdelaziz, A., et al. Mapping fracture complexity of fractured shale in laboratory: Three-dimensional reconstruction from serial-section images. Rock Mechanics and Rock Engineering, 2022a, 55(5): 2937-2948.

Li, G., Song, X., Tian, S., et al. Intelligent drilling and completion: A review. Engineering, 2022b, 18: 33-48.

Liu, G., Ehlig-Economides, C. Practical considerations for diagnostic fracture injection test (DFIT) analysis. Journal of Petroleum Science and Engineering, 2018, 171: 1133-1140.

Liu, G., Ehlig-Economides, C. Comprehensive before-closure model and analysis for fracture calibration injection falloff test. Journal of Petroleum Science and Engineering, 2019, 172: 911-933.

Liu, L., Guo, X., Wang, X., et al. Integrated wellbore-reservoir-geomechanics modeling for enhanced interpretation of distributed fiber-optic strain sensing data in hydraulic-fracture analysis. Journal of Rock Mechanics and Geotechnical Engineering, 2024, 16(8): 3136-3148.

Liu, Y., Jin, G., Wu, K., et al. Hydraulic-fracture-width inversion using low-frequency distributed-acoustic-sensing strain data – Part I: Algorithm and sensitivity analysis. SPE Journal, 2021, 26(1): 359-371.

Maxwell, S. Microseismic Imaging of Hydraulic Fracturing: Improved Engineering of Unconventional Shale Reservoirs. Houston, USA, Society of Exploration Geophysicists, 2014.

Manjunath, G. L., Liu, Z., Jha, B. Multi-stage hydraulic fracture monitoring at the lab scale. Engineering Fracture Mechanics, 2023, 289: 109448.

McCormack, K. L., Zoback, M. D., Kuang, W. A case study of vertical hydraulic fracture growth, stress variations with depth and shear stimulation in the Niobrara Shale and Codell Sand, Denver-Julesburg Basin, Colorado. Interpretation, 2021, 9(4): SG59-SG69.

Mondal, S., Zhang, M., Huckabee, P., et al. Advancements in step down tests to guide perforation cluster design and limited entry pressure intensities – Learnings from field tests in multiple basins. Paper SPE 204147 Presented at SPE Hydraulic Fracturing Technology Conference and Exhibition, Virtual, 3-5 May, 2021.

Nayak, A., Correa, J., Ajo-Franklin, J. Seismic magnitude estimation using low-frequency strain amplitudes recorded by DAS arrays at far-field distances. Bulletin of the Seismological Society of America, 2024, 114(4): 1818-1838.

Nguyen, K., Zhang, M., Ayala, L. Transient pressure behavior for unconventional gas wells with finite-conductivity fractures. Fuel, 2020, 266: 117119.

Nolte, K. Determination of fracture parameters from fracturing pressure decline. Paper SPE 8341 Presented at SPE Annual Technical Conference and Exhibition, Las Vegas, Nevada, 23-26 September, 1979.

Parisio, F., Yoshioka, K., Sakaguchi, K., et al. A laboratory study of hydraulic fracturing at the brittle-ductile transition. Scientific Reports, 2021, 11(1): 22300.

Pei, Y., Sepehrnoori, K. Investigation of parent-well production induced stress interference in multilayer unconventional reservoirs. Rock Mechanics and Rock Engineering, 2022, 55: 2965-2986.

Ren, Z., Yan, R., Huang, X., et al. The transient pressure behavior model of multiple horizontal wells with complex fracture networks in tight oil reservoir. Journal of Petroleum Science and Engineering, 2019, 173: 650-665.

Sun, Z., Zhao, Y., Gao, Y., et al. Effects of bedding characteristics on crack propagation of coal under mode II loading: Laboratory experiment and numerical simulation. Journal of Rock Mechanics and Geotechnical Engineering, 2025, 17(2): 1037-1052.

Tripoppoom, S., Wang, X., Liu, Z., et al. Characterizing hydraulic and natural fractures properties in shale oil well in Permian basin using assisted history matching. Fuel, 2020, 275: 117950.

Unal, E., Rezaei, A., Siddiqui, F., et al. Improved understanding of dynamic fracture behavior in unconventional horizontal wells using wavelet transformation. Paper SPE 195889-MS Presented at SPE Annual Technical Conference and Exhibition, Calgary, Alberta, Canada, 30 September-2 October, 2019.

Wang, Z., Cai, Y., Liu, D., et al. Characterization of natural fracture development in coal reservoirs using logging machine learning inversion, well test data and simulated geostress analyses. Engineering Geology, 2024, 341: 107696.

Wang, Y., Hu, X., Zhou, F., et al. Comparing different segments in shut-in pressure signals: New insights into frequency range and energy distribution. Petroleum Science, 2025, 22(1): 442-456.

Wei, Z., Sheng, M., Hu, Z., et al. Identification of nearly pure leak-off phase from pressure falloff curve and its interpretation on fracture areas. SPE Journal, 2024, 29(11): 6185-6197.

Wei, Z., Sheng, M., Hu, Z., et al. Acoustic signatures of sonar-based fracture diagnostics in horizontal wells. Physics of Fluids, 2025, 37(8): 083116.

Wu, K., Liu, Y., Jin, G., et al. Fracture hits and hydraulic-fracture geometry characterization using low-frequency distributed acoustic sensing strain data. Journal of Petroleum Technology, 2021, 73(7): 39-42.

You, S., Liao, Q., Yue, Y., et al. Enhancing fracture geometry monitoring in hydraulic fracturing using radial basis functions and distributed acoustic sensing. Advances in Geo-Energy Research, 2025, 16(3): 260-275.

Zhang, R., Chen, M., Zhao, Y., et al. Production performance simulation of the fractured horizontal well considering reservoir and wellbore coupled flow in shale gas reservoirs. Energy & Fuels, 2022, 36(22): 13637-13651.

Zoback, M., Kohli, A. Unconventional Reservoir Geomechanics. Cambridge, UK, Cambridge University Press, 2019.